

Journal of Materials Chemistry C

Accepted Manuscript



This is an *Accepted Manuscript*, which has been through the Royal Society of Chemistry peer review process and has been accepted for publication.

Accepted Manuscripts are published online shortly after acceptance, before technical editing, formatting and proof reading. Using this free service, authors can make their results available to the community, in citable form, before we publish the edited article. We will replace this *Accepted Manuscript* with the edited and formatted *Advance Article* as soon as it is available.

You can find more information about *Accepted Manuscripts* in the [Information for Authors](#).

Please note that technical editing may introduce minor changes to the text and/or graphics, which may alter content. The journal's standard [Terms & Conditions](#) and the [Ethical guidelines](#) still apply. In no event shall the Royal Society of Chemistry be held responsible for any errors or omissions in this *Accepted Manuscript* or any consequences arising from the use of any information it contains.

Cite this: DOI: 10.1039/c0xx00000x

www.rsc.org/xxxxxx

ARTICLE TYPE

The combinations of hollow MoS₂ micro@nano-spheres: one-step synthesis, excellent photocatalytic and humidity sensing properties

Yinghua Tan,^a Ke Yu,^{*a} Ting Yang,^a Qingfeng Zhang,^a Weitao Cong,^a Haihong Yin,^a Zhengli Zhang,^a Yiwei Chen,^b and Ziqiang Zhu^a

Received (in XXX, XXX) Xth XXXXXXXXX 20XX, Accepted Xth XXXXXXXXX 20XX
DOI: 10.1039/b000000x

The combinations of hollow MoS₂ micro@nano-spheres were successfully fabricated through a one-step hydrothermal method. A possible growth mechanism was presented in detail based on time-dependent experimental facts. Besides, the photocatalytic activities of the samples were evaluated by monitoring the photodegradation of methylene blue (MB). The adsorption value of 150 mg/g shows a strong adsorption capability in dark. After irradiation for only 30 min, the remaining MB in solution is about 9.7%. Moreover, the humidity sensing properties of the samples were measured for the first time. The results revealed high sensitivity at high RH, small humidity hysteresis, fast response and recovery time, and good stability. The greatest sensitivity is 32.19 nF/ % RH and the maximum hysteresis is ~6.3% RH. For humidity cycling of 17.2%–89.5%–17.2% RH, the response and recovery time are ~140 s and ~80 s, respectively. Capacitance fluctuations for one month are less than ±7% under various relative humidity (RH).

1. Introduction

In recent decades, two-dimensional (2D) layered nanomaterials such as graphene have aroused increasing research interest in industrial and scientific fields because of their unique properties and wide potential applications.^{1–6} MoS₂, resembling graphene, a typical example of two-dimensional (2D) layered nanomaterials, has attracted great attention for its layered structure, in which each layer consists of molybdenum atoms sandwiched between two layers of hexagonally close-packed sulfur atoms.^{7, 8} The adjacent atomic sandwiches are held together by weakly van der Waals forces.⁹ As a transition metal sulfide, MoS₂ possesses many excellent properties and is widely applied in many fields such as super solid lubricants,⁷ lithium battery cathodes,^{10–12} sensors,^{13–17} photocatalysis,^{18–20} hydrogen storage medias,^{21, 22} and dye-sensitized solar cells²³ etc. To date, a great deal of efforts have been devoted to the MoS₂ studies and all kinds of chemical and physicochemical methods, including hydrothermal method,^{24, 25} gas-phase synthesis,²⁶ electrochemical deposition²⁷, thermal decomposition²⁸, chemical vapour deposition²⁹ and electrochemical based Li-intercalation method³⁰ were put forward to synthesize MoS₂ with various morphologies, such as fullerene-like nanoparticles,²⁶ hollow microspheres,³¹ nanotubes,²¹ nanorods,³² nanowires,³³ nanoflowers.²⁴ But it is still a challenge to fabricate various novel combinations of MoS₂ with the controlled sizes via a facile and effective method. Herein, we first report the fabrication of hollow MoS₂ micro@nano-spheres through a one-step hydrothermal method. Moreover, the growth process and a possible formation mechanism of the samples were preliminarily presented on the basis of the experimental facts by

adjusting the reaction time.

Generally, the overall photocatalytic activities of semiconductive materials are mainly decided by three factors: (1) The adsorption ability of photocatalysis, (2) the separation and transporting rate of the photogenerated holes and electrons for the existence of active surfaces (sites) in catalysts, (3) photoabsorption ability in the available light energy region.³⁴ MoS₂ with various morphologies previously reported have prospective applications in photocatalysts and the energy gap of MoS₂ nanomaterials is close to 1.78 eV, with a strong absorption in the visible light region to improve the utilization of sunlight.^{19, 35} Therefore, it is certainly worth investigating the photocatalytic activities of this hollow MoS₂ micro@nano-spheres. Besides, MoS₂ is also an ideal candidate material for gas sensors, such as hydrogen sensors, which evidence by theoretical results¹⁴ and recent experiments³⁶. However, few researches on humidity sensing property of MoS₂ nanostructure have been deeply reported so far.

Hence the photocatalytic activities of the novel hollow MoS₂ micro@nanocrystals were examined in our paper. The reason of the strong adsorption capability and excellent photocatalytic activity for organic pollutants under visible light illumination were discussed. Furthermore, the humidity sensing performances of the MoS₂-based sensors were investigated for the first time and the results indicate that the sensors possess pronounced sensitivity in high RH environment, very small humidity hysteresis, fast response and recovery time, and good stability. A theoretical explanation of the humidity sensing property is also given in our research.

2. Experimental section

2.1 Synthesis of hollow MoS₂ micro@nano-spheres

In our experiments, all chemicals were analytical grade and used directly without further purification. The combinations of hollow MoS₂ micro@nano-spheres were fabricated through a one-step hydrothermal route in Teflon-lined autoclaves. The preparation procedure was described as follows: 0.4 g thioacetamide (C₂H₅NS) and 0.2 g sodium molybdate (Na₂MoO₄·2H₂O) as Mo and S sources, respectively, were dissolved in 60 ml deionized water to form a transparent solution, and then 0.5 g oxalic acid (H₂C₂O₄) was added into the above solution to adjust the pH value. After magnetic stirring for 30 min, a homogeneous solution was obtained and transferred into a Teflon-lined stainless-steel autoclave. The autoclave was heated at 200 °C for 22 h in an electric oven. After naturally being cooled down to room temperature, black precipitates were collected, washed sequentially by sonication for 10 min with deionized water and ethanol for several times, and finally dried at 60 °C for 6 h to obtain the black powders. To obtain MoS₂ with good crystallinity, the as-prepared samples were annealed under an atmosphere of Ar at 800 °C for 2 h in a conventional tube furnace.

2.2 Characterization

The crystal structure of the products was characterized by X-ray diffraction (XRD, Bruker D8 Advance diffractometer) with Cu K α radiation ($\lambda=1.5418$ Å). The diffraction patterns were collected in the 2θ scanning range of 10–80° with 0.02° per step. The morphologies and structures of the samples were examined by field emission scanning electron microscopy (FESEM, JEOL-JSM-6700F) at an accelerating voltage of 20 kV, and transmission electron microscopy (TEM, Jeol, JEM-2100) at an accelerating voltage of 200 kV. All measurements for the as-prepared samples were carried out at room temperature. The samples for TEM analysis were obtained by adding a drop of the colloidal solution onto a standard holey carbon-coated copper grid. The grids were dried in air at room temperature.

2.3 Photocatalytic measurements

The photocatalytic properties of the as-prepared samples were investigated by the degradation of methylene blue (MB) aqueous solution. The concentration of the extracted MB solution was tested by monitoring the absorbance at the major absorption peak (663 nm). Before illumination, the suspension containing as-prepared MoS₂ (0.01 g) and 120 mL of 20 mg L⁻¹ MB aqueous solution by one experiment was treated by sonication for 6 min and then magnetically stirred in the dark for 20 min to ensure the establishment of the adsorption/desorption equilibrium. 4 mL of the suspension was withdrawn and clarified by centrifugation at 800 rpm for 10 min to remove the residual catalyst. Then the clarified solution was analyzed by a UV-vis spectrophotometer (UNICO 2802) to evaluate the adsorption ability. For photocatalytic degradation measurements, the suspension was illuminated by an 18 W daylight lamp (20 cm above the reactor) used as a solar-simulated light source. To minimize the heat effect, the reactor was implemented in a big glass container, cooled by flowing water at room temperature. The aliquots (4 mL) of the suspension were clarified and analysed after 10-min

periodic intervals of irradiation, during the total 60-min irradiation time. For comparison, the various initial concentrations of MB (25 mg L⁻¹, 15 mg L⁻¹, and 10 mg L⁻¹) were used in the adsorption testes.

2.4 Preparation of sensors for humidity measurement

A MoS₂-based humidity sensor is constructed with an interdigitated-type electrode and MoS₂ film on the surface of a glass sheet substrate in the inset of Fig. 7c. The glass sheet substrate (12 cm × 16 cm × 0.5 cm) was cleaned in a sonication bath for 5 min, and the interdigitated-type silver paste electrodes with the width of ~0.5 mm and ~3 mm electrode gaps was deposited on the glass substrate. The Ag electrodes are the electrodes of the double-layer capacitance. The MoS₂ suspension was dispersed by ultrasonic method and deposited by dip coating on the glass substrate with the electrode to form a thin film as a humidity sensing layer. Then the configuration was dried at 50 °C for 6 h. The controlled humidity environments, 23, 43, 57, 75, 80, 85, 93% RH, were achieved using saturated aqueous solution of CH₃COOK, K₂CO₃, NaBr, NaCl, KBr, KCl, and KNO₃ at room temperature, respectively. These saturate salt solutions were placed in JKZ1 Radiosonde Ground Check to provide uniform and stable humidity environments. Different humidity environments result in different effective dielectric constants which lead to different capacitances. In the capacitance measurement, the equipment we used was the Precision LCR Meter TH2817A with frequency of 100 kHz from China Tonghui.

3. Results and discussion

3.1 Structure characterization

The XRD patterns of annealed and unannealed samples are shown in Fig. 1(a). It is obvious that the as-prepared MoS₂, after annealed in Ar at 800 °C, exhibits high crystallinity compared with unannealed samples. The observed diffraction peaks at $2\theta = 14.4^\circ, 33.1^\circ, 39.7^\circ$ and 58.5° can be assigned to the (002), (100), (103) and (110) planes of the hexagonal phase MoS₂ with lattice constants $a=b=0.316$ nm, $c=1.229$ nm (Molybdenite, JCPDS card no.37-1492), respectively. Besides the very weak diffraction peaks at $2\theta = 37^\circ$ and 53.5° can be suitably indexed to monoclinic MoO₂, which reveals that the annealed samples is MoS₂ containing trace amounts of MoO₂ impurity. This may be due to the existence of trace oxygen in the process of high-temperature annealing. The XRD pattern of the as-obtained unannealed samples only displays two weak diffraction peaks, (002) and (100), and the others characteristic peaks do not appear, which indicates poor crystallinity of the samples and makes it difficult to identify its phase. This poor-stacked structure can be explained by the tensile force and randomness of the amorphous samples.³¹ In addition, it is worth noticing that a new diffraction peak, marked with blue line circles in Fig. 1(a)B, is found near $2\theta=10^\circ$ which could not be indexed to MoS₂. The new peak may be due to the reflection from two adjacent single-layer amorphous MoS₂³⁷ or the greater distance of unannealed MoS₂ layers,¹¹ which possibly associated with the strain/stress caused by the bending and folding of the amorphous layers.³⁸ While annealed samples exhibit high crystallinity and a strong diffraction peak (002) at $2\theta=14.4^\circ$ with an interlayer spacing of 0.62 nm in Fig. 1(a) A, which indicates that the layered MoS₂ grow well along

the c axis. Therefore, the crystallinity of the MoS_2

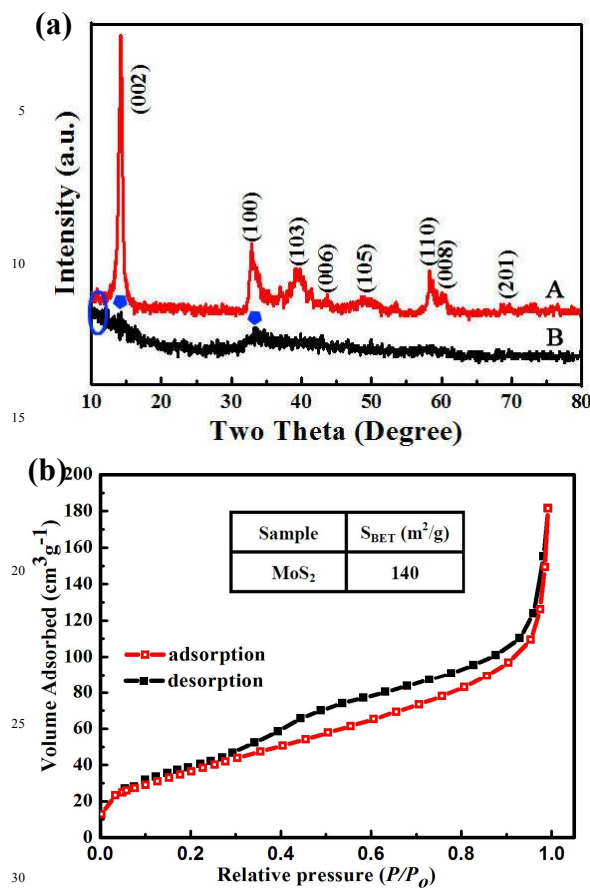


Fig. 1 (a) X-ray patterns of (A) annealed samples (B) unannealed samples. (b) Nitrogen adsorption/desorption isotherms of hollow MoS_2 micro@nano-spheres. The table in the inset is the S_{BET} for the samples.

samples prepared by hydrothermal route could be improved by annealing at high temperature and the strain/stress achieved readjustment to lead the disappearance of the diffraction peak near $\sim 10^\circ$. From the N_2 adsorption/desorption isotherm (Fig. 1(b)), a distinct hysteresis loop is identified at a relative pressure of 0.1–0.9, demonstrating the presence of a mesoporous structure, which leads to a Brunauer-Emmett-Teller (BET) surface area of $140 \text{ m}^2 \text{ g}^{-1}$.

The size and morphology of the as-synthesized MoS_2 were primarily characterized by SEM images under different magnifications. In Fig. 2a and b, it is very obvious that the obtained products are composed of microspheres and nanospheres with the diameters of $\sim 1 \mu\text{m}$ and $\sim 200 \text{ nm}$, respectively, called combinations of hollow MoS_2 micro@nano-spheres. Additionally, every microsphere is dispersedly surrounded by nanospheres. The numbers of these microspheres and nanospheres are relatively coordinated in the hydrothermal process, which makes this micro@nano-structure look uniform and coordinated. The inset of Fig. 2b and Fig. 2c clearly show the surfaces of these nanospheres and microspheres. The rough surfaces with abundant weak burrs are scraggly. The typical contact interface between a microsphere and a nanosphere distinctly confirm that microspheres and nanospheres grow into wholes during the hydrothermal process in the inset of Fig. 2c. As presented in Fig. 2c and d, several broken microspheres indicate

that microspheres are hollow and the thicknesses of the

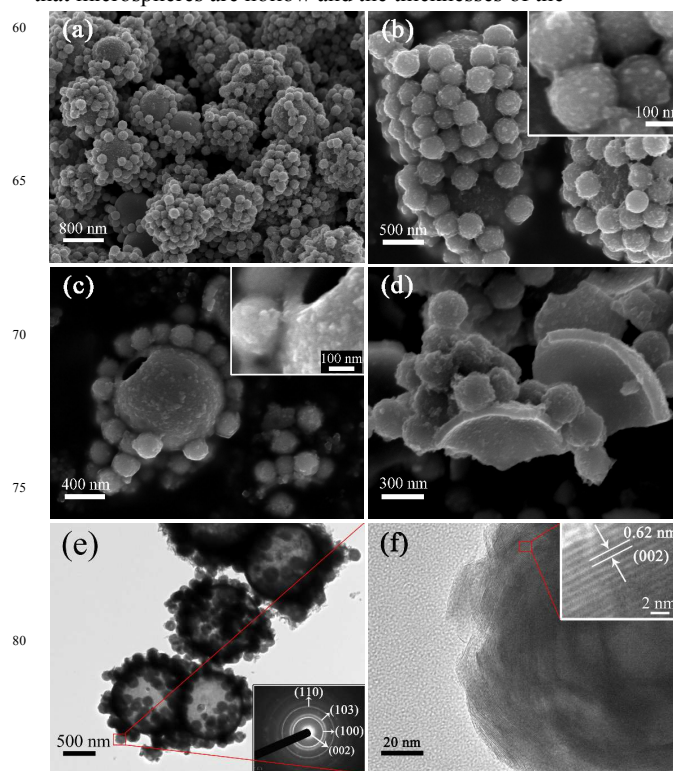


Fig. 2 (a) Low magnification SEM image. (b) Medium magnification SEM image. The inset is the high magnification SEM image of several typical nanospheres surfaces. (c) The SEM image of a microsphere surface. The inset is the HRSEM of the typical contact interface between a microsphere and a nanosphere. (d) The SEM image of several broken microspheres. (e) The TEM image of the typical samples. Lower inset is the corresponding selected area electron diffraction (SAED) pattern. (f) The high-resolution TEM image of a nanosphere, the red rectangular area in e. Upper inset is the HRTEM image corresponding to the red rectangular area.

microspheres shell are about 40 nm , only about a fourteenth of the diameter of a hollow microsphere, which demonstrates the microspheres shells are very thin and fragile.

The structure of the samples was further characterized by TEM and high-resolution TEM (HRTEM) images. Fig. 2e presents a typical TEM image of several microspheres surrounded by nanospheres. The significant contrast between the edges and centres of the microspheres further confirms the hollow structure feature. Fig. 2f is the HRTEM image of the red rectangular area in Fig. 2e. Some defects and faults are observed on the surface of the nanosphere, which lead to the rough surfaces with abundant weak burrs and pits. The rough surfaces of microspheres, resembling nanospheres, should also be due to the abundant defects and faults, which can increase the specific surface area to improve various performances, such as adsorption capacity and photocatalytic activity etc. It should be noted that the nanospheres obviously consist of several layers. There is a distinction difference between the middles and edges in the nanospheres structure. Compared with the edges, the internal streaks were observably less and even none, suggesting the nanospheres structure are virtually the spherical shell with a little centrally cavity and can be regarded as a nestification of several spheres.

This structure is similar to ‘Russian doll’ or ‘onion’ structure³¹

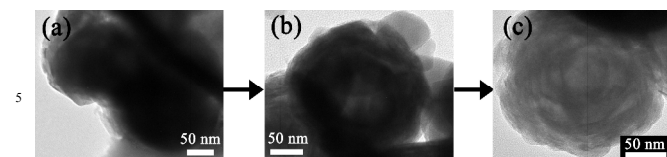
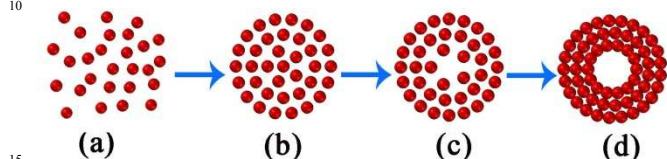


Fig. 3 TEM images aimed at disclosing the growth process of nanospheres by interrupting the reaction at different time (a) 2 h, (b) 6 h, (c) 10 h.



Scheme 1 The schematic demonstration of the proposed formation mechanism of MoS₂ nanospheres

and very crucial to understand its formation mechanism. The HRTEM image in the inset, corresponding to the red rectangular area in Fig. 2f, presents the lattice fringes of the samples with the well-defined crystal structure, and the lattice spacing, assigned to the (002) plane, is about 0.62 nm. The inset in Fig. 2e illustrates the corresponding selected area electron diffraction (SAED) rings arise from the stacking of MoS₂ with different crystallographic orientations. The central bright spot corresponds to the (002) plane and the observed separated diffraction rings correspond to the (100), (103) and (110) planes, respectively, which is consistent with the XRD result.

3.2 The time-dependent possible formation mechanism

Generally, the formation of nanomaterials with different morphologies may be related to the characteristics of amorphous primary particles and nucleation in different reaction conditions.³⁹ Besides, the reaction time of the hydrothermal process is crucial to the growth of morphologies. Therefore, the temporal evolution of the products is monitored by TEM and SEM to shed light on the morphological evolution and formation mechanism of the hollow MoS₂ micro@nano-spheres. Firstly, we proposed a possible growth mechanism for nanospheres in Scheme 1, which was drawn based on the TEM of temporal evolution in Fig. 3. Scheme 1 actually reveals a similar Ostwald ripening self-assembly process with a fast nucleation of amorphous primary particles.⁴⁰ Prior to heating, numerous amorphous primary MoS₂ nanoparticles, symbolized by the red globules in Scheme 1, were generated in the reaction solution. After heating to a certain temperature, these amorphous primary MoS₂ nanoparticles spontaneously and quickly aggregated into evacuating solid spheres and then evolved with respectively layered spherical shells. The amorphous nanoparticles located in the centre of the solid spheres were incompact and less dense than those in the outer parts. When prolonging reaction time, it was found that the amorphous MoS₂ particles in the internal layered spherical shells were transferred to the outer parts, resulting in a small void in the centre and shorter distance between the spherical layers. With the time sequentially increasing, the central void became larger and well-crystallized layered spherical shells were located at the outer parts. The ‘onion’ structure with a little cavity was finally formed.

Additionally, to further gain insight into the growth process

and formation mechanism of the hollow micro@nano-spheres,

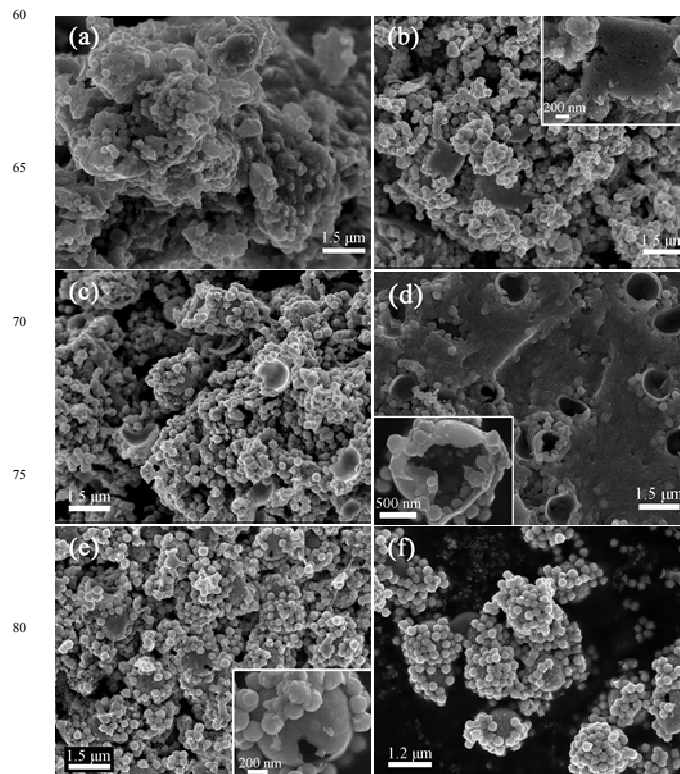
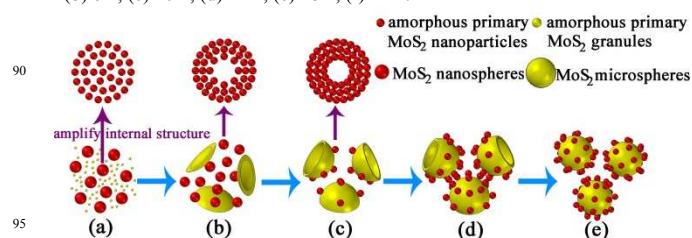


Fig. 4 SEM images aimed at disclosing the growth process of MoS₂ micro@nano-spheres by interrupting the reaction at different time. (a) 2 h, (b) 6 h, (c) 10 h, (d) 14 h, (e) 18 h, (f) 22 h.



Scheme 2 The schematic demonstration of the proposed formation mechanism of the hollow MoS₂ micro@nano-spheres.

keeping other typical parameters unchanged, time-dependent experiments at different reaction times (2 h, 6 h, 10 h, 14 h, 18 h, 22 h) were conducted and monitored by SEM images of the obtained products in Fig. 4. When the reaction time was 2 h, microspheres cannot be found and the product only consisted of nanospheres and abundant granules (Fig. 4a) which may be the amorphous primary particles to form microspheres. More granules may lose during the process washing. Prolonging reaction time to 6 h, many small cambered pieces were observed in Fig. 4b and the high-magnification SEM image in the inset of Fig. 4b clearly shows a typical cambered piece with small fissures and the loose aggregation of granules. When the reaction time was increased to 10 h, the trend of cambered growth became more obvious. As illustrated in Fig. 4c, the size of the cambered surface was about a third of the microsphere. After time reaching for 14 h, the size of the cambered shell became greater than a half of the microsphere. The thin edges of a typical cambered shell reveal the growth direction in the inset of Fig. 4d. Meanwhile, some nanospheres attached on these cambered surfaces to grow

into the whole in Fig. 4d, where black motes was the amorphous primary granules without washed away to form MoS₂ microspheres. With further increase of the reaction time to 18 h, the shell almost grew into a sphere except for a small hole and more nanospheres sequentially attached on the new growth spherical shell, which was observed in Fig. 4e. The high-magnification SEM image in the inset of Fig. 4e clearly shows a typical small hole on the microsphere. After the time reached to 22 h, hollow MoS₂ micro@nano-spheres were eventually formed in Fig. 4f. In the growth process, reaction time is the most significant controlling factor.

Based on our experimental facts, the proposed schematic of the growing process of the hollow micro@nano-spheres is depicted in Scheme 2. In the first stage, the previously discussed evacuating solid nanospheres and the amorphous primary MoS₂ granules, symbolized by big red balls and smaller yellow balls, respectively, were initially formed during the temperature of 200 °C for 2 h. Different from amorphous primary MoS₂ particles generated at room temperature to form nanospheres, these amorphous primary MoS₂ granules were generated during high temperature via the reaction of remainder solute and in a stronger acidic solution because of the increasing hydrolysis of undecomposed Oxalic acid. Due to the effect of low concentration, high temperature, stronger acidic solution, these amorphous granules with different surface free energy did not aggregate into small spheres through the Ostwald ripening process. Instead, the earlier amorphous granules were spontaneously oriented and aggregated to form many tiny cambered pieces with amorphous and poorly crystallized phase. With the increase of reaction time, the later amorphous granules, formed during the continually decreasing concentration of solute, were transferred toward the previous cambered pieces and grew along with the cambered pieces, reported by K. H. Hu et al.⁴¹, which resulting in the growth of cambered pieces further to larger pieces. Simultaneously, nanospheres were formed on the surfaces of these cambered pieces due to the reassembly aggregation and distribution between nanospheres and the new growing cambered surfaces. As the reaction time was sequentially prolonged and the aging process continued, evacuating solid nanosphere gradually evolved into the 'onion' structure and these cambered pieces nearly became hollow microspheres. Meanwhile, nanospheres attached on the new growth cambered surfaces. Finally, the combinations of hollow MoS₂ micro@nano-spheres were perfectly formed. On the basis of the above results, we reach a conclusion that the formation mechanism of nanospheres is the similar to the Ostwald ripening with a fast self-assembly nucleation and slow evolution process. Nevertheless, the growth process of the microspheres was the growth of amorphous granules along with the spherical surfaces. Two kinds of growth process are simultaneous. Eventually, microspheres and nanospheres grow into well-dispersed wholes.

3.3 Photocatalytic activities

Methylene blue (MB) with a major absorption peak at 663nm is one of the most common contaminant in industrial waste water and used to estimate the adsorption abilities and photodegradation activities of the as-prepared samples. The changes in the absorption spectra of the extracted MB solution in the presence of the MoS₂ samples were shown in Fig. 6a. For comparison, the

supernatant of MoS₂ solution without MB was carried out (

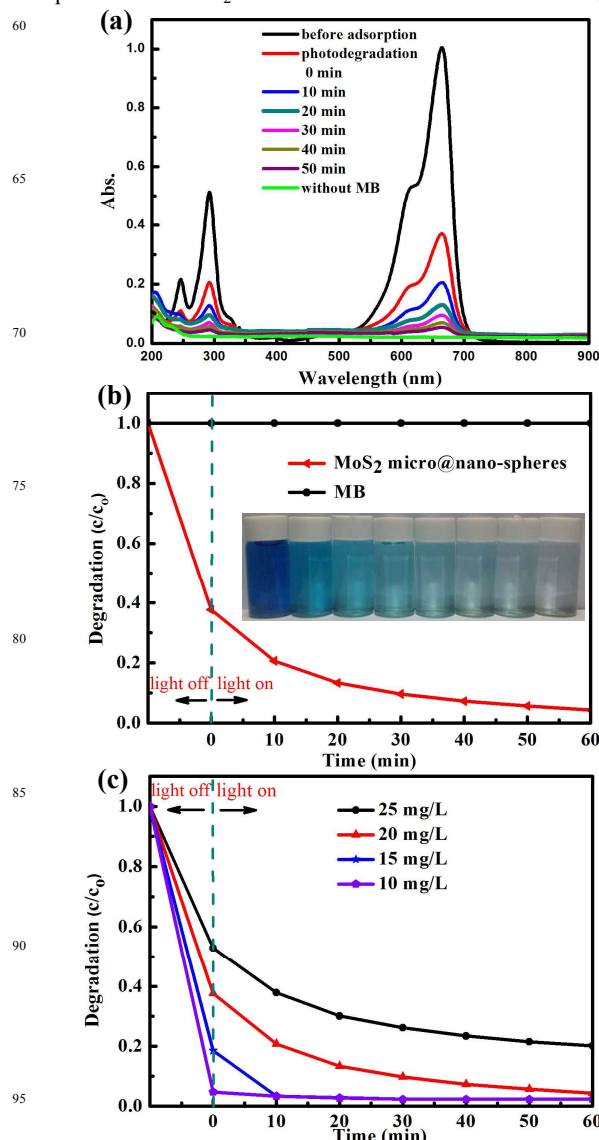


Fig. 5 (a) Absorption spectra of the MB solution under visible light irradiation in the presence of the MoS₂ samples. (b) Degradation rates of MB with and without photocatalyst as a function of irradiation time. (c) Degradation rates of MB with photocatalyst versus the different initial concentrations.

green line in Fig. 5a), accounting for the absorption spectra (750 nm-900nm) above zero except for main peaks. The continuous reduction of the absorption intensity at 663 nm indicates the gradually decreasing concentration of MB with the extended irradiation time. The dependency of the degradation rate on irradiation time is revealed in Fig. 5b, where C and C_0 stand for the remnants and initial concentration of MB, respectively. A compared photodegradation experiment on the degradation of pristine MB solution without photocatalysts was performed and almost no photocatalytic decolorization of MB after irradiating for 1 h was shown by the black line in Fig. 5b. Therefore, MoS₂ play an essential role for efficient dye degradation under the visible light illumination. Before the light irradiation, the mixed solution of MoS₂ and MB was stirred in dark to establish the adsorption/desorption equilibrium of MB on the samples surfaces. Dramatically, the remaining MB in solution is about

37.6%, indicating that the MoS₂ samples present strong adsorption ability

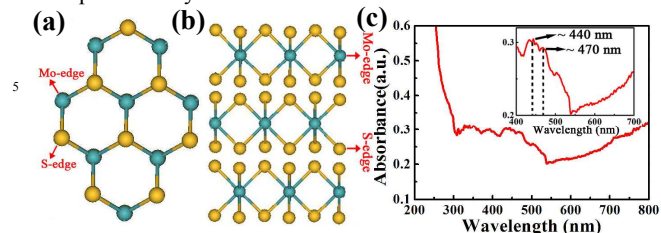
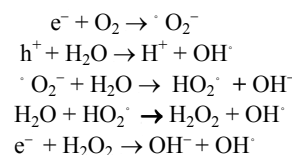


Fig. 6 (a) The top view of the hexagonal MoS₂ crystallite exposing Mo- and S-edges. (b) The side view of the hexagonal MoS₂ crystallite exposing Mo- and S-edges. (c) UV-Vis spectra of the samples. The inset shows an expanded view for the Visible light region.

towards the MB, with the adsorption value of 150 mg/g in dark. This is possibly due to the large specific surface area which can adsorb the abundant dye molecules¹⁸. Moreover, according to the previous data, the MoS₂ samples evidently exhibit very high photodegradation activities in the photodegradation of MB. After irradiation for only 30 min, the C/C₀ rapidly dropped to 9.7% and MB was almost completely degraded under 60-min light irradiation. This result is also consistent with the colour change of the suspension from blue to colourless. In order to determine the favourable exploitation rate and reveal the effect of the initial concentration of MB on the degradation rate, Fig. 5c shows a comparison of the various initial concentrations of MB aqueous solutions. It can be clearly seen that the degradation rate gradually decreased when the initial concentration increased. Interestingly, when the initial concentration of MB is less than 20 mg/L the strong adsorption ability play a major role to remove dye molecules. Photodegradation capacity is not fully utilized which implies a lower utilization rate for the photocatalyst.

The excellent photocatalytic performance of the as-prepared samples is attributed to not only the large specific surface area but also the scraggly surfaces of MoS₂ micro@nano-spheres with abundant weak burrs and a strong absorption in the visible light region. It is generally accepted that the large specific surface area can improve adsorption capacity for dye molecules and bring more unsaturated surfaces coordination sites exposed to the MB molecules. To the best of our knowledge, the rim and edge sites of MoS₂ are the active sites for the HDS reaction based on the 'rim-edge' mode.⁴² As shown in Fig. 6a and b, every S atom coordinates two Mo atoms on the S-edge and every Mo atom coordinates four S atoms on the Mo-edge. Mo- and S-edges with dangling bonds are unstable and would strongly interact with positively charged MB molecules.⁴³ Herein, the scraggly surfaces with abound defects and faults can provide vast rim and edge active sites for the degradation of MB. Additionally, Fig. 6c shows that MoS₂ samples have an observable absorbance at ~ 440 nm and ~ 470 nm in the visible light region. Thurston and Wilcoxon also reported that the absorption peak of MoS₂ (d=4.5nm) is at ~ 470 nm.³⁵ Electrons from the valence band of MoS₂ absorb visible light and transfer to the conduction band to produce separated electron-hole pairs. The photoexcited electrons were scavenged by the oxygen in the water and valence band holes were adsorbed by water molecules, which can form hydroxyl radicals(.OH) to photooxidize organic molecules.³⁵ A possible mechanism accounting for ·HO production can be written as⁴⁴:



Furthermore, the existence of broken microspheres cannot be excluded among the samples because of the thin spherical shells, which brings about more rim and edge active sites and improves the degradation rate of MB. We believe this kind of attractive materials with high adsorption abilities and excellent photocatalytic performances will have promising application in the water treatment to remove toxic heavy metal ions and degrade dye pollutants.

3.5 Humidity sensing properties

The humidity sensing property of the MoS₂-based sensor was evaluated through discussing humidity sensitivity, hysteresis, response and recovery time, and stability under various relative humidity (RH). The sensor capacitance as a function of RH was presented by red line in Fig. 7a during the adsorption process. It can be observed that the output capacitance exponentially increase with the RH. When RH changed from 17.2% to 52.8%, the relative capacitance only increased from 89.25 pF to 96.36 pF, a fairly small increment. Nevertheless, as RH varied from 71.8% to 89.5%, the relative capacitance dramatically rose from 0.504 nF to 6.01 nF, exhibiting pronounced sensitivity in high RH environment. To quantitatively illustrate its humidity sensitivity, the sensitivity is defined as $\Delta c/\Delta RH$ (%), the ratio of the change in output capacitance against the change in RH, and the sensitivity values at different RH can be seen clearly in the inset of Fig. 7a. It is found that the greatest sensitivity is 32.19 nF/%RH (at RH=89.5%) which confirms high sensitivity in high RH environment. Hysteresis is an important parameter for evaluating the performance of a humidity sensor. Fig. 7a also illustrates the hysteresis property of the as-fabricated sensor by increasing the RH from 10% to 98% for water molecules adsorption and then decreasing back to 10% for water molecules desorption. From the narrow humidity loop curve, the differences between output capacitances in the adsorption and desorption process are obviously small under all humidity conditions. The maximum hysteresis was ~6.3% RH occurred at 71.8% RH which exhibits good reversible characteristic. Further the dynamic testing of the sensing device was carried out to investigate more parameters including response and recovery time, and reproducibility at 25 °C. Fig. 7b shows the time-dependent response and recovery curves (corresponding to water molecules adsorption and desorption processes). During humidity cycling of 17.2%–71.8%–17.2% RH the response and recovery time (defined as the time reached 95% of the final steady capacitance value) are ~90 s and ~110 s, respectively. For 17.2%–89.5%–17.2% RH cycling, the response time and recovery time are ~140 s and ~80 s, respectively. The results indicate fast response behaviour for humidity sensing. Moreover, three cycles demonstrate good reproducibility of the sensor. To test the stability, the sensor was exposed in air for 30 days and the measurements were repeated every 2 days at different RH. It can be observed that the capacitances fluctuations are less than ±7% at relevant humidity region and the sensitivity variation for one month is also small in the inset of Fig. 7a, which directly

confirms the good stability and reliability. Therefore, MoS₂ micro@nano-spheres are expected to be potential material for

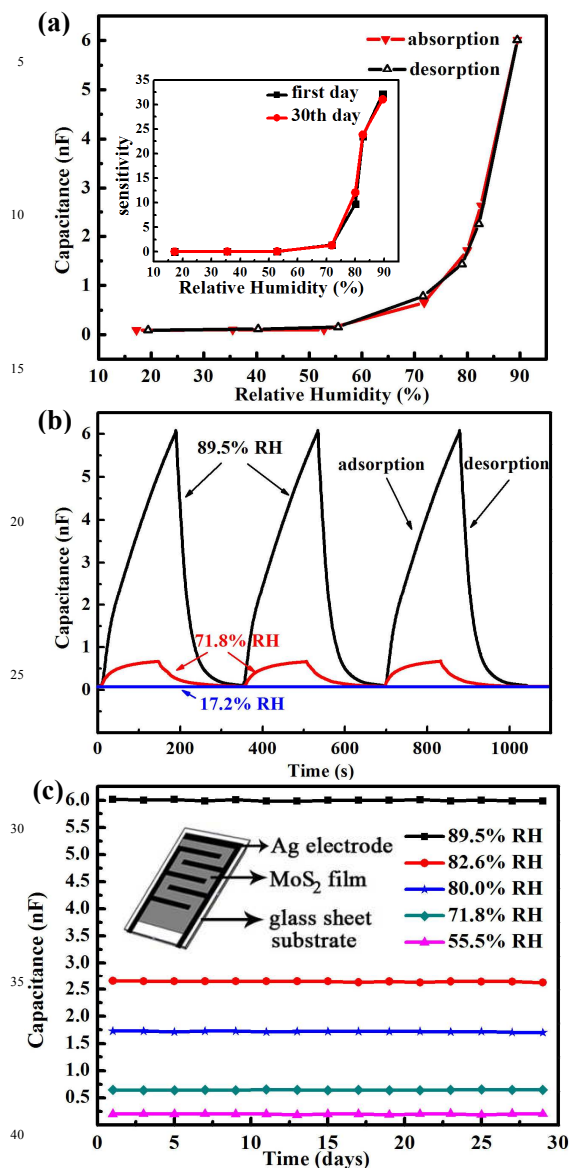


Fig. 7 (a) Experimental capacitance-RH response and hysteresis loop curve of the as-fabricated sensor. The inset is the defined sensitivity at different RH. (b) The response and recovery times under humidity cycling of 17.2%-71.8%-17.2% RH and 17.2%-89.5%-17.2% RH. (c) Capacitance variations at various RH levels in 30 days. The inset is a schematic diagram of the as-fabricated sensor.

high humidity sensors.

The humidity sensitive performances of MoS₂-based humidity sensors may be mainly attributed to the large specific surface area of the samples, which can increase the moisture adsorption capacity and facilitate the release of water molecules. The humidity sensing mechanism of the MoS₂ samples is the charge transfer between H₂O molecules and MoS₂ surfaces, which has been previously reported by Q. Yue et al.¹⁴ A large number of H₂O molecules are continually physis-orbed on the MoS₂ surfaces with the increment of RH, and H₂O molecules are preferably adsorbed on the top of hexagons (in Fig. 8a).^{14, 45} Electron charges are sequentially transferred from the MoS₂

surfaces to H₂O molecules as charge acceptors (in Fig. 8b). Consequently, the free electrons on the MoS₂ film are decreasing

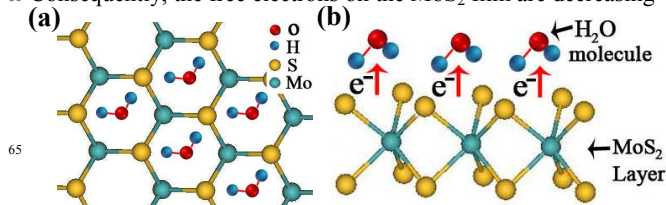


Fig. 8 (a) The top view of the most favorable configurations for H₂O molecules on the MoS₂ film. (b) The schematic image of the humidity sensing mechanism.

during the adsorption process, which increasing the dielectric constant. As we know, the capacitance is positively proportional to the dielectric constant and the reciprocal of the thickness of the double layer electrodes. The thickness of the double layer electrodes is constant in the testing process. So the capacitance increased with the dielectric constant. At low RH, the probability of contact between water molecules and MoS₂ surfaces is low⁴⁶ and water molecules cannot form continuous water layers. Hence, the transfer of H₂O or H₃O⁺ on the discontinuous water layer is difficult⁴⁷ and the sensor exhibits lower sensitivity. As the RH is increased, several serial water layers emerge on the MoS₂ surfaces and the physisorbed water can be ionized by an electrostatic field into abundant H₃O⁺ as charge carries.⁴⁸ The rapidly transfer of H₂O or H₃O⁺ on the free water layers possibly transport electrons to outer water layers via the conductivity sharply accelerating the decrease of the electron density on the MoS₂ surfaces, which result in a high sensitivity at high RH. Furthermore, the dielectric constant of hydrated water is 2.2 and free water is 78, which also raise output capacitance and enhance the sensor sensitivity at high RH.⁴⁸

4. Conclusion

In summary, the combinations of hollow MoS₂ micro@nano-spheres were successfully synthesized through a one-step hydrothermal method. A possible formation mechanism was discussed. In addition, the samples possess strong adsorption capabilities in dark and excellent photocatalytic activities under visible light illumination. We believe this kind of attractive materials will have promising application in the water treatment to remove toxic heavy metal ions and degradation dye pollutants. The humidity sensing properties of the samples were measured for the first time, and the results indicated high sensitivity at high RH, small humidity hysteresis, fast response and recovery time, and good stability. A humidity sensing mechanism is also given in our research. Therefore, the hollow MoS₂ micro@nano-spheres can be a promising candidate for high humidity sensors applications in the future.

Acknowledgments

The authors acknowledge financial support from the NSF of China (Grant Nos. 61204018, 61274014), Innovation Research Project of Shanghai Education Commission (Grant No. 13zz033), Education Committee of Jiangsu Province (Grant No. 12KJD510011), and Project of Key Laboratory of Polar Materials and Devices (Grant No. KFKT2014003).

Notes and references

^a Key Laboratory of Polar Materials and Devices (Ministry of Education of China), Department of Electronic Engineering, East China Normal University, Shanghai, 200241, P. R. China. Fax: +86-21-54345198; Tel: +86-21-54345198; E-mail: yk5188@263.net

^b Department of Physics, East China Normal University, Shanghai, 200241, P. R. China.

1. C. N. Rao, A. K. Sood, K. S. Subrahmanyam and A. Govindaraj, *Angew Chem Int Ed Engl*, 2009, 48, 7752-7777.
2. R. Mas-Balleste, C. Gomez-Navarro, J. Gomez-Herrero and F. Zamora, *Nanoscale*, 2011, 3, 20-30.
3. X. Cao, Z. Yin and H. Zhang, *Energy & Environmental Science*, 2014, DOI: 10.1039/c4ee00050a.
4. Q. He, S. Wu, Z. Yin and H. Zhang, *Chemical Science*, 2012, 3, 1764-1772.
5. Z. Yin, J. Zhu, Q. He, X. Cao, C. Tan, H. Chen, Q. Yan and H. Zhang, *Advanced Energy Materials*, 2014, 4, n/a-n/a.
6. X. Huang, Z. Zeng, Z. Fan, J. Liu and H. Zhang, *Advanced Materials*, 2012, 24, 5979-6004.
7. M. R. Hilton, R. Bauer, S. V. Didiulis, M. T. Dugger, J. M. Keem and J. Scholhamer, *Surface and Coatings Technology*, 1992, 53, 13-23.
8. M. Chhowalla, H. S. Shin, G. Eda, L.-J. Li, K. P. Loh and H. Zhang, *Nat Chem*, 2013, 5, 263-275.
9. R. Tenne, L. Margulis, M. Genut and G. Hodes, *Nature*, 1992, 360, 444-446.
10. S. Ding, D. Zhang, J. S. Chen and X. W. Lou, *Nanoscale*, 2012, 4, 95-98.
11. S. K. Park, S. H. Yu, S. Woo, B. Quan, D. C. Lee, M. K. Kim, Y. E. Sung and Y. Piao, *Dalton Trans*, 2013, 42, 2399-2405.
12. X. Cao, Y. Shi, W. Shi, X. Rui, Q. Yan, J. Kong and H. Zhang, *Small*, 2013, 9, 3433-3438.
13. Q. He, Z. Zeng, Z. Yin, H. Li, S. Wu, X. Huang and H. Zhang, *Small*, 2012, 8, 2994-2999.
14. Q. Yue, Z. Shao, S. Chang and J. Li, *Nanoscale Res Lett*, 2013, 8, 1-7.
15. C. Zhu, Z. Zeng, H. Li, F. Li, C. Fan and H. Zhang, *Journal of the American Chemical Society*, 2013, 135, 5998-6001.
16. S. Wu, Z. Zeng, Q. He, Z. Wang, S. J. Wang, Y. Du, Z. Yin, X. Sun, W. Chen and H. Zhang, *Small*, 2012, 8, 2264-2270.
17. H. Li, Z. Yin, Q. He, H. Li, X. Huang, G. Lu, D. W. H. Fam, A. I. Y. Tok, Q. Zhang and H. Zhang, *Small*, 2012, 8, 63-67.
18. W. Zhou, Z. Yin, Y. Du, X. Huang, Z. Zeng, Z. Fan, H. Liu, J. Wang and H. Zhang, *Small*, 2013, 9, 140-147.
19. K. H. Hu, X. G. Hu, Y. F. Xu and X. Z. Pan, *Reaction Kinetics, Mechanisms and Catalysis*, 2010, DOI: 10.1007/s11144-010-0173-3.
20. Z. Yin, B. Chen, M. Bosman, X. Cao, J. Chen, B. Zheng and H. Zhang, *Small*, 2014, DOI: 10.1002/smll.201400124, n/a-n/a.
21. J. Chen, S. L. Li and Z. L. Tao, *Journal of Alloys and Compounds*, 2003, 356-357, 413-417.
22. J. Chen, N. Kuriyama, H. Yuan, H. T. Takeshita and T. Sakai, *Journal of the American Chemical Society*, 2001, 123, 11813-11814.
23. G. Yue, J. Wu, Y. Xiao, M. Huang, J. Lin and J.-Y. Lin, *Journal of Materials Chemistry A*, 2013, 1, 1495.
24. Q. Zhang, K. Yu, B. Zhao, Y. Wang, C. Song, S. Li, H. Yin, Z. Zhang and Z. Zhu, *RSC Advances*, 2013, 3, 10994.
25. C.-B. Ma, X. Qi, B. Chen, S. Bao, Z. Yin, X.-J. Wu, Z. Luo, J. Wei, H. Zhang and H. Zhang, *Nanoscale*, 2014, DOI: 10.1039/c3nr04975b.
26. A. Zak, Y. Feldman, V. Alperovich, R. Rosentsveig and R. Tenne, *Journal of the American Chemical Society*, 2000, 122, 11108-11116.
27. E. A. Ponomarev, M. Neumann-Spallart, G. Hodes and C. Lévy-Clément, *Thin Solid Films*, 1996, 280, 86-89.
28. C. M. Zelenski and P. K. Dorhout, *Journal of the American Chemical Society*, 1998, 120, 734-742.
29. X. Wang, H. Feng, Y. Wu and L. Jiao, *Journal of the American Chemical Society*, 2013, 135, 5304-5307.
30. Z. Zeng, Z. Yin, X. Huang, H. Li, Q. He, G. Lu, F. Boey and H. Zhang, *Angewandte Chemie International Edition*, 2011, 50, 11093-11097.
31. G. Li, C. Li, H. Tang, K. Cao, J. Chen, F. Wang and Y. Jin, *Journal of Alloys and Compounds*, 2010, 501, 275-281.
32. M. A. Albitar, R. Huirache-Acuna, F. Paraguay-Delgado, J. L. Rico and G. Alonso-Nunez, *Nanotechnology*, 2006, 17, 3473-3481.
33. W.-J. Li, E.-W. Shi, J.-M. Ko, Z.-z. Chen, H. Ogino and T. Fukuda, *Journal of Crystal Growth*, 2003, 250, 418-422.
34. Z. Ai, L. Zhang, S. Lee and W. Ho, *The Journal of Physical Chemistry C*, 2009, 113, 20896-20902.
35. T. R. Thurston and J. P. Wilcoxon, *The Journal of Physical Chemistry B*, 1998, 103, 11-17.
36. B. Miremadi, R. Singh, S. R. Morrison and K. Colbow, *Appl. Phys. A*, 1996, 63, 271-275.
37. Z. Wang, L. Ma, W. Chen, G. Huang, D. Chen, L. Wang and J. Y. Lee, *RSC Advances*, 2013, 3, 21675.
38. M. Wang, G. Li, H. Xu, Y. Qian and J. Yang, *ACS Applied Materials & Interfaces*, 2013, 5, 1003-1008.
39. H. Shi, K. Yu, F. Sun and Z. Zhu, *CrystEngComm*, 2012, 14, 278-285.
40. H. Chun Zeng, *Current Nanoscience*, 2007, 3, 177-181.
41. K. H. Hu and X. G. Hu, *Materials Science and Technology*, 2009, 25, 407-414.
42. M. Daage and R. R. Chianelli, *Journal of Catalysis*, 1994, 149, 414-427.
43. V. M. Kogan and P. A. Nikulshin, *Catalysis Today*, 2010, 149, 224-231.
44. S. Li, K. Yu, Y. Wang, Z. Zhang, C. Song, H. Yin, Q. Ren and Z. Zhu, *CrystEngComm*, 2013, 15, 1753-1761.
45. F. K. Perkins, A. L. Friedman, E. Cobas, P. M. Campbell, G. G. Jernigan and B. T. Jonker, *Nano Letters*, 2013, 13, 668-673.
46. H. Yin, K. Yu, Z. Zhang, M. Zeng, L. Lou and Z. Zhu, *Electroanalysis*, 2011, 23, 1752-1758.
47. W.-D. Lin, H.-M. Chang and R.-J. Wu, *Sensors and Actuators B: Chemical*, 2013, 181, 326-331.
48. H. Bi, K. Yin, X. Xie, J. Ji, S. Wan, L. Sun, M. Terrones and M. S. Dresselhaus, *Sci. Rep.*, 2013, 3.

Graphical Abstract

The combinations of hollow MoS_2 micro@nano-spheres were successfully fabricated through a one-step hydrothermal method. The combinations of hollow MoS_2 micro@nano-spheres possess a strong adsorption capability and an excellent photocatalytic activity towards dye molecules, which attributed to the large specific surface area, the curved basal surfaces with abound burrs, and a strong absorption in the visible light region. Moreover, the MoS_2 -based sensor exhibits high sensitivity at high RH.

